Composite Structures 304 (2023) 116304

Contents lists available at ScienceDirect

Composite Structures

journal homepage: www.elsevier.com/locate/compstruct

Study on mechanical properties of lattice structures strengthened by synergistic hierarchical arrangement

Ruiyao Liu [a], Guofeng Yao [a], Kuiyang Gao [a], Zezhou Xu [b], Yanan Yang [b], Xue Guo [b], Zhenglei Yu [b,c,*], Zhihui Zhang [c], Chunyang Han [d]

[a] Department of Mechanics, School of Mechanical and Aerospace Engineering, Jilin University, Changchun 130022, China
[b] Key Lab of Bionic Engineering, Ministry of Education, Jilin University, Changchun 130022, China
[c] State Key Laboratory of Automotive Simulation and Control, Jilin University, Changchun 130022, China
[d] Changchun Institute of Optics, Fine Mechanics and Physics, Chinese Academy of Sciences, Changchun 130022, China

ARTICLE INFO

Keywords:
Hierarchical lattice structures
Synergistic effect
The global simulated annealing algorithm
Constitutive relations

ABSTRACT

To study the synergistic hierarchical arrangement effect, three hierarchical cubic lattice structures and six kinds of hybrid hierarchical lattice structures are designed based on the synergistic hierarchical arrangement concept. While studying the synergistic hierarchical arrangement effect on the structural protection characteristics, the prediction function of structural properties and the constitutive relation of lattice structures are derived. The structural properties are accurately predicted, and the errors are within 5%. In terms of mechanical properties of lattice structures, 941 hybrid hierarchical lattice structure, similar to the hybrid hierarchical arrangement inside the femur, presents the best mechanical behavior, followed by 194 and 419 hybrid hierarchical lattice structure. The bearing capacity, specific energy absorption, and energy absorption of 941 are more than 100% of those of other hierarchical or synergistic hybrid hierarchical lattice structures. The results show that the hierarchical and synergistic hybrid hierarchical lattice structure can effectively improve the mechanical properties of the lattice structure in different directions, especially the femur-like synergistic hybrid hierarchical structure. To better determine the excellent performance of the hybrid hierarchical structure, combined with the car seat, the performance of the hybrid hierarchical structure is further studied. Ideas are provided for the subsequent application of energy-absorbing engineering.

1. Introduction

In recent years, passenger transport safety engineering has been concerned with the increase in collision accidents in passenger transport engineering [1–3]. How to ensure the safety of personnel to the greatest extent under limited cost has become a research hotspot nowadays [4–6]. In the process of a car accident, it is essential to improve the survival rate of passengers by absorbing the composite direction energy through the energy absorption device of the safety seat. The porous structure in the energy-absorbing unit of the seat is a critical energy-absorbing part of the seat. Previous studies have mainly focused on the optimal design of structure cells and the selection of fabrication materials. In comparison, few studies have been done on the energy absorption effect of safety seats through the functional properties of the structure in the assembly of multiple types of lattice structures.

Organisms have acquired powerful energy absorption properties by utilizing their excellent microstructure, which has aroused the great attention of researchers [7–9]. Subsequently, the lattice cell structures of biological bone structures [10–12] and their microscopic compositions [13–15] have been studied extensively. Chen et al. [16] selected representative volume cells of shell and aragonite fiber based on the observation of shell microstructure. They analyzed the mechanism of aragonite fiber microstructure characteristics to obtain high stiffness and strength of the shell. Kooistra et al. [17] introduced the bionic hierarchy idea into the bionic corrugated sandwich structure and brought the two-level corrugated sandwich structure (two-level folded structure). The plane stress hypothesis and elastic beam theory proposed six dominant failure modes of the structure. Katayama et al. [18] established a biomimetic composite model with honeycomb structure based on the microstructure characteristics of cancellous bone. They used this model to predict and analyze the optimization mechanism of compressive stress diffusion. These research results show that bionic design

* Corresponding author at: Key Lab of Bionic Engineering, Ministry of Education, Jilin University, Changchun 130022, China.
E-mail address: zlyu@jlu.edu.cn (Z. Yu).

https://doi.org/10.1016/j.compstruct.2022.116304
Received 30 June 2022; Accepted 5 October 2022
Available online 21 October 2022

based on natural biological composite materials can improve the mechanical properties of composite structures in engineering.

However, in manufacturing complex porous structures, traditional manufacturing methods cannot meet the manufacturing needs of these complex structures. The emergence of additive manufacturing technology provides an effective way for the manufacturing application of complex structures [19–21]. Yan et al. [22] prepared a series of $AlSi_{10}Mg$ diamond porous lattice structures using SLM technology. They found that the mechanical properties of $AlSi_{10}Mg$ diamond porous lattice structures formed by SLM were highly controllable. The mechanical properties of porous lattice structures could be controlled effectively by controlling the single-cell size and volume fraction. To compare the mechanical properties of different porous lattice structures, Maskey et al. [23] manufactured a porous lattice structure with gradient density by fixing the average relative density of the porous lattice structure at 22 % and studied the mechanical behavior of uniform porous lattice structure and gradient porous lattice structure. Gorny et al. [24] manufactured Ti6Al4V porous lattice structure using additive manufacturing technology and studied the microstructure, deformation behavior, and failure mechanism of the porous lattice structure.

In this study, the mechanical properties of hierarchical and hybrid hierarchical lattice structures are compared. Based on the same-sized hierarchical lattice cells, the hierarchical lattices (primary hierarchical lattice structure 111, secondary hierarchical lattice structure 444, and tertiary hierarchical lattice structure 999) are composed for studying the effect of hierarchical cubic configuration on the overall mechanical properties of lattice structures. Next, to study the impact of the hybrid hierarchical arrangement on the mechanical properties, the hierarchical lattice structures are arranged firstly and combined to form the hybrid hierarchical lattice structures: 149, 194, 419, 491, 914, 941. The expressions for the names of the hybrid hierarchical lattice structures are explained using the hybrid hierarchical lattice structures 941 and primary cubic lattice structure 111 as examples, as shown in Fig. 1(c). To study the mechanical properties of lattice structures in the composite direction, the compression of oblique 45 degrees to the x-axis, x-direction, and z-direction mechanical properties of lattice structures are reviewed. Ultimately, the mechanical properties of lattice structures are summarized by comparing simulations, experiments, and theories. The findings are described. The effect of structural synergistic hierarchical arrangement on mechanical properties is described in detail.

2. Lattice specimen preparation

The design of hierarchical lattice structures is based on the same-sized hierarchical cubic lattice cells of aperture scaling as the prototype. Three types of hierarchical lattice structures are designed, as shown in Fig. 1 (c). The 3D printing machine FS403P is used to manufacture PA300 Nylon hierarchical lattice samples.

The biological femur can effectively protect the human body [25]. The internal hybrid hierarchical composition of the femur is divided into three layers: compact bone, bone marrow, and spongy bone, as shown in Fig. 2 (a). To further explore the effect of the hybrid hierarchical arrangement of the femur on mechanical properties, the hybrid hierarchical lattice structures consist of hierarchical lattice cells surrounded from inside to outside: 149 hybrid hierarchical lattice structure, 194 hybrid hierarchical lattice structure, 419 hybrid hierarchical lattice structure, 491 hybrid hierarchical lattice structure, 914 hybrid hierarchical lattice structure, and 941 hybrid hierarchical lattice structure, as shown in Fig. 2 (a_1- c_1) (a_2- c_2). Based on six hybrid hierarchical lattice structures, the effect of synergistic hierarchical arrangement on the structural protective performance is studied under different loading directions.

Since 3D printing parameters significantly influence the mechanical properties of lattice structures when the 3D printing machine FS403P manufactures lattice structures [26], the unified printing parameters are used in this paper to test more accurate properties of lattice structures. The 3D printer printing parameters are in Table 1.

In comparing the lattice structures simulation, it is necessary to set the structural material parameters. As LS-DYNA #24 material can be directly entered into the material tensile curve for material parameter setting, lattice structure simulations are carried out with #24 material. To determine the material properties of lattice structures, the mechanical experiments at room temperature are conducted on the DDL100 testing machine. The tensile and compression force–displacement curves of Nylon samples are in Fig. 3.

3. Grid sensitivity analysis of the hierarchical lattice cell

Structural grid sensitivity analysis is performed to ensure the accuracy of simulation analysis. The convergence analysis, under the four different cell sizes of 0.5 mm, 0.75 mm, 1 mm, and 1.5 mm, is done for CB1, CB2, and CB3, as shown in Fig. 4.

It is seen from Fig. 4 that the force–displacement curves of cubic lattice elements obtained at the sizes of 0.5 mm, 0.75 mm, and 1 mm are close to each other numerically, which indicates convergence of simulation calculations. The 0.5 mm adaptive mesh refinement method is used for structure simulation analysis to improve the accuracy and speed of simulation analysis.

4. Theory analysis of lattice structures

4.1. Mechanical properties analysis of lattice structures

The lattice structure exhibits elastic deformation at the initial stage of compression. Under the meager structural strain rate, that is, quasi-static compression, Euler beam theory can be used to calculate the deformation of the lattice structure whose relative density ρ/ρ_S is more significant than 0.1 [27]. According to the Euler beam theory, the micro-deformation of a structural beam is.

$$\Delta L = \frac{FL^3}{E_S I} \tag{1}$$

$$I = \frac{t^4}{12} \tag{2}$$

where, E_S is the elastic modulus of Nylon. t is the width of the structural beam. L is the length of structural beam.

The structural elastic modulus is.

$$E = \frac{\sigma}{\varepsilon} = \frac{E_S I}{\zeta_1 S L^2} \tag{3}$$

where,

$$\sigma = \frac{F}{S} = \frac{\Delta L E_S I}{S L^3} \tag{4}$$

$$\varepsilon = \frac{\Delta L}{L} \tag{5}$$

The structural relative density is.

$$\frac{\rho}{\rho_S} = \frac{M/V}{M/V_S} = \frac{V_S}{V} \tag{6}$$

where, $V_S \propto Lt^2, V = L^3$, ρ is the solid density of the lattice structure. ρ_S is the material density of Nylon.

$$\frac{\rho}{\rho_S} \propto \left(\frac{t}{L}\right)^2 \tag{7}$$

Thus,

$$\frac{E}{E_S} \propto \left(\frac{\rho}{\rho_S}\right)^2 \tag{8}$$

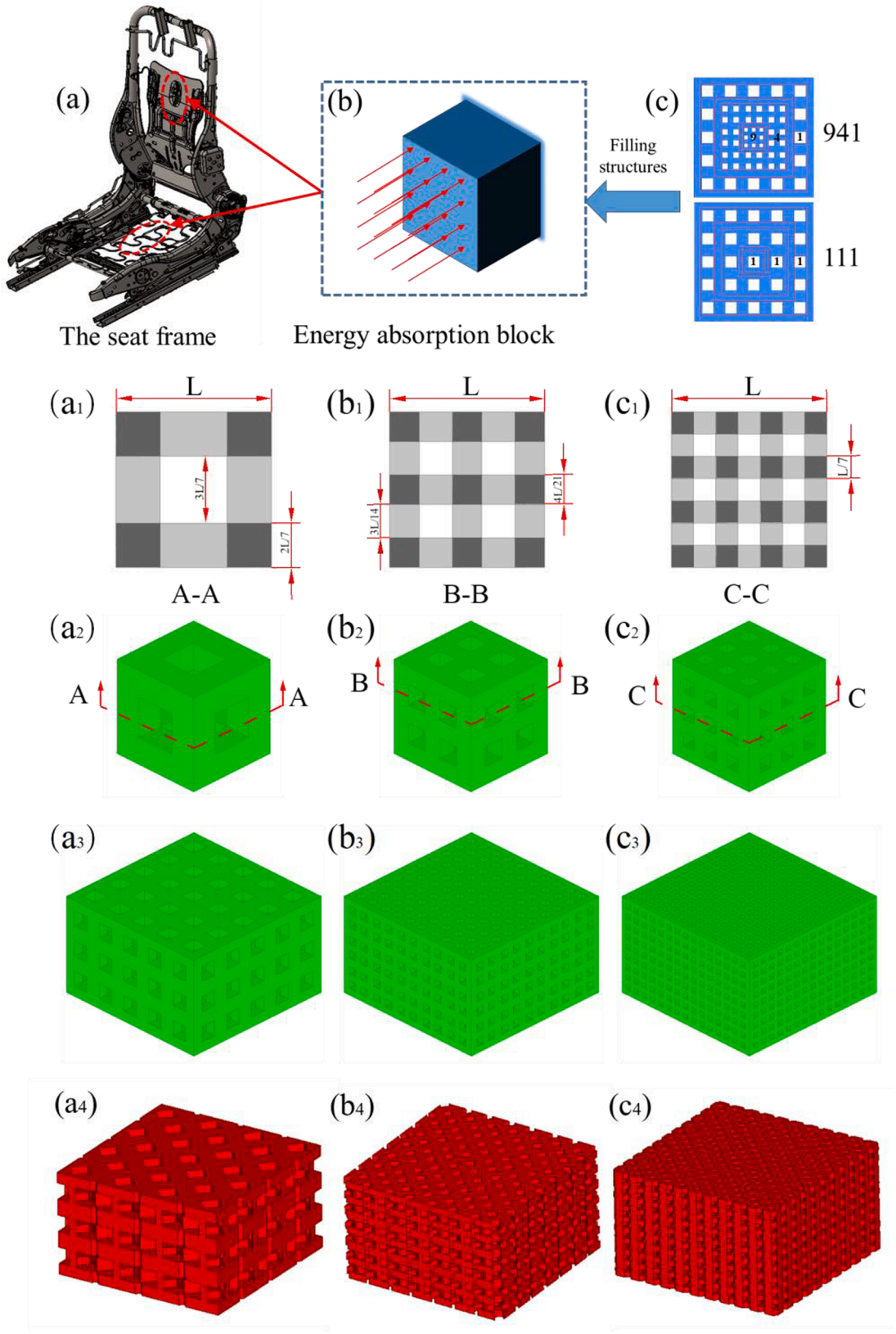

Fig. 1. Energy absorption lattice structures of the car safety seat. (a) The safety seat. (b) Energy absorption block. (c) Energy absorption lattice structure. (a_1), (b_1), and (c_1) are the sectional view of CB1, CB2, and CB3. $L = 7$ mm. (a_2) CB1, (b_2) CB2, and (c_2) CB3 are the hierarchical lattice cells that make up 111, 444, and 999. (a_3) primary hierarchical lattice structure 111. (b_3) secondary hierarchical lattice structure 444. (c_3) tertiary hierarchical lattice structure 999. (a_4) oblique 45 degrees to the x-axis primary hierarchical lattice structure 111. (b_4) oblique 45 degrees to the x-axis secondary hierarchical lattice structure 444. (c_4) oblique 45 degrees to the x-axis tertiary hierarchical lattice structure 999.

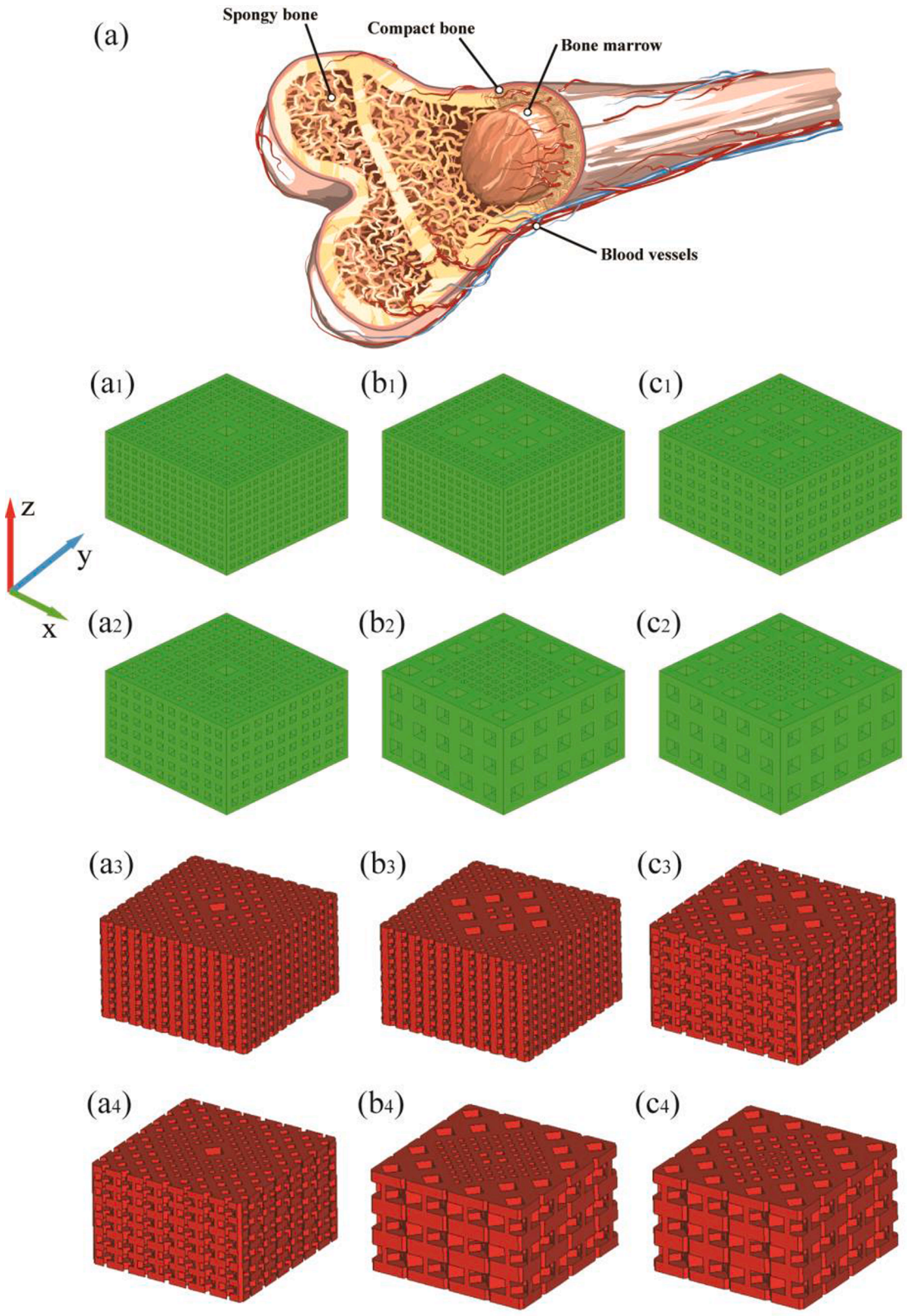

Fig. 2. Hybrid hierarchical lattice structures. (a) Hierarchical structures of the femur. In the femur, compact bone is equivalent to CB1. Spongy bone is equal to CB2. Bone marrow is matching to CB3. (a_1) 149 hybrid hierarchical lattice structure. (b_1) 419 hybrid hierarchical lattice structure. (c_1) 914 hybrid hierarchical lattice structure. (a_2) 194 hybrid hierarchical lattice structure. (b_2) 491 hybrid hierarchical lattice structure. (c_2) 941 hybrid hierarchical lattice structure. (a_3) 149 oblique 45 degrees to the x-axis hybrid hierarchical lattice structure. (b_3) 419 oblique 45 degrees to the x-axis hybrid hierarchical lattice structure. (c_3) 914 oblique 45 degrees to the x-axis hybrid hierarchical lattice structure. (a_4) 194 oblique 45 degrees to the x-axis hybrid hierarchical lattice structure. (b_4) oblique 45 degrees to the x-axis 491 hybrid hierarchical lattice structure. (c_4) 941 oblique 45 degrees to the x-axis hybrid hierarchical lattice structure.

Table 1
FS 403P 3D-printing parameters.

Parameters	Scanning speed (mm/s)	Build cavity temperature (°C)	Laser power (W)	Preheating temperature (°C)	Jumping speed (mm/s)	Material
Tensile sample	7.62	169	22	140	2.54	PA300

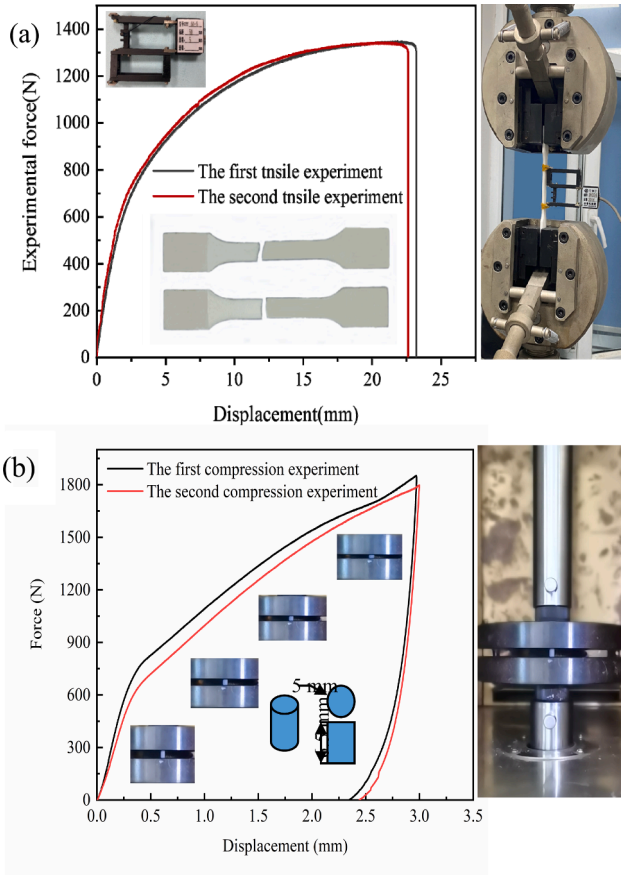

Fig. 3. Nylon properties curve. (a) Nylon tensile curve. The parallel length of the tensile samples is 60 mm. The gauge length of tensile samples is 50 mm, and the thickness of tensile samples is 4 mm. (b) Nylon compression curve.

That is.

$$\frac{E}{E_S} = A_1\left(\frac{\rho}{\rho_S}\right)^2 + B_1 \tag{9}$$

where, A_1 and B_1 are the constants.

The relationship between relative elastic modulus and relative density of lattice structures in this paper is shown in Fig. 5(a).

The Euler formula determines the bending force.

$$F = \frac{n^2\pi E_S I}{L^2} \tag{10}$$

where, n is the degree of freedom of structural constraints. In the lattice structures, $n = 0.7$ [27].

Therefore, the lattice structures are stressed when bending deformation under compression.

$$\sigma \propto \frac{F}{L^2} \propto \frac{E_S I}{L^4} \tag{11}$$

Combine (2) and (7),

$$\frac{\sigma}{E_S} \propto \frac{t^4}{L^4} \propto \left(\frac{\rho}{\rho_S}\right)^2 \tag{12}$$

That is.

$$\frac{\sigma}{E_S} = A_2\left(\frac{\rho}{\rho_S}\right)^2 + B_2 \tag{13}$$

where, A_2 and B_2 are the constants.

The relationship between bending stress and the relative density of lattice structures in this paper is shown in Fig. 5(b).

4.2. Improving constitutive relation of lattice structures

In terms of functional properties, the porous lattice structures are similar to the porous material in terms of mechanical properties. It can be obtained by analogy from previous research on the compression of porous material that the compression force of the lattice structures can be divided into three stages: elastic stage, plastic stage, and dense stage [27], as shown in Fig. 7.

$$\sigma = \begin{cases} E\varepsilon, \sigma \leqslant \sigma_y \\ \sigma_y, \varepsilon_y \leqslant \varepsilon \leqslant \varepsilon_D\left(1 - D^{-1}\right) + \varepsilon_y \\ \sigma_y \frac{1}{D}\left(\frac{\varepsilon_D}{\varepsilon_D - \varepsilon}\right)^m, \varepsilon > \varepsilon_D\left(1 - D^{-1}\right) + \varepsilon_y \end{cases} \tag{14}$$

where, σ is the structural stress. ε is the structural strain. E is the elastic modulus. σ_y is the structural yield stress. ε_y is the strain when structural yield occurs. ε_D is the strain when the structure is dense. D and m are constants.

To simplify the loaded relationship and better describe the stress–strain relationship, Rush Model [28] was proposed.

$$\sigma = A\varepsilon^m + B\varepsilon^n, \quad 0 < m < 1 \quad and \quad 1 < n < \infty \tag{15}$$

where, the first term on the right side of the equation represents the elastic segment, and the second term means the plastic stage. Although the proposed model simplifies the whole compression constitutive model, its accuracy in describing the compaction stage is insufficient.

When considering strain rate, the constitutive compression relation of the porous structure can be obtained by analogy with the latest constitutive relation of porous material [29].

$$\sigma = f(\varepsilon)M(\varepsilon, \dot{\varepsilon}) \tag{16}$$

where, σ is the structural stress. $f(\varepsilon)$ is the shape function of strain, representing the stress–strain relationship at the reference strain rate, generally expressed by a polynomial. It is a function of the strain and the strain rate. The quasi-static compression strain rate is constant. $M(\varepsilon, \dot{\varepsilon}) = \left(\frac{\dot{\varepsilon}}{\dot{\varepsilon}_0}\right)^{a+b\varepsilon} = 1$[30]. Introduce the Avalle improved constitutive model [31].

$$\sigma = f(\varepsilon) = A\left(1 - e^{-(E/C)\varepsilon(1-\varepsilon)^m}\right) + B\left(\frac{\varepsilon}{1-\varepsilon}\right)^n \tag{17}$$

where, σ is the structural stress. ε is the structural strain. E is the elastic modulus. A, B,C, m and n are constants.

However, in the process of compression, the lattice structure has a local failure, and the stress will mutate. Therefore, the fracture failure factor $C(\varepsilon)$ is introduced in this paper, and Eq. (18) is.

$$\sigma = C(\varepsilon)f(\varepsilon) \tag{18}$$

Firstly, to improve the computational efficiency and increase the accuracy, the $f(\varepsilon)$ model and the Rush model are improved.

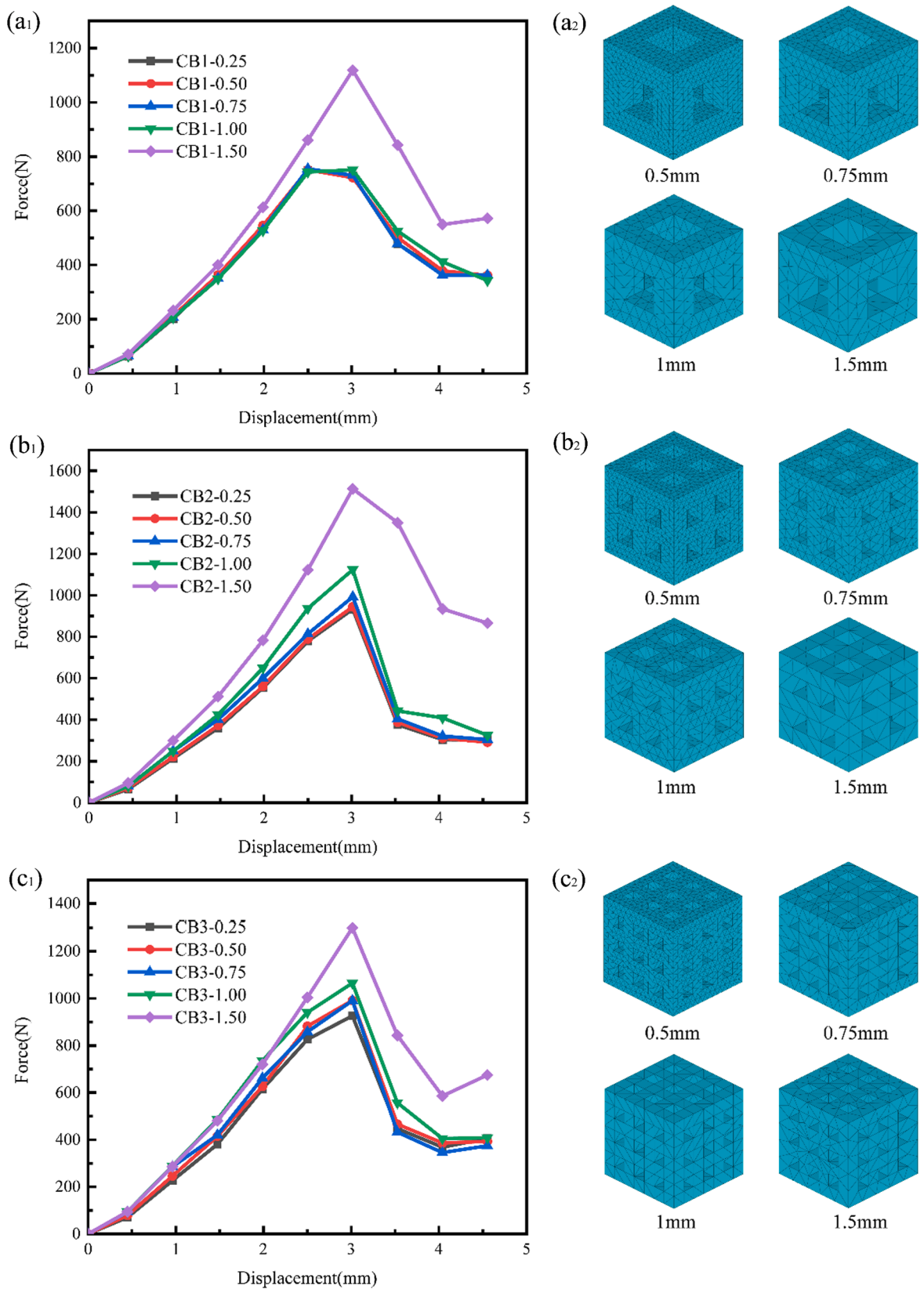

Fig. 4. Structural grid sensitivity analysis. (a_1) first-order cubic cell (CB1), and force–displacement curve. (b_1) second-order cubic cell (CB2) force–displacement curve. (c_1) third-order cubic cell (CB3) force–displacement curve. (a_2) CB1 is divided into four grid sizes: 0.5 mm, 0.75 mm, 1 mm and 1.5 mm (b_2) CB2 is divided into four grid sizes: 0.5 mm, 0.75 mm, 1 mm and 1.5 mm. (c_2) CB3 is divided into four grid sizes: 0.5 mm, 0.75 mm, 1 mm and 1.5 mm.

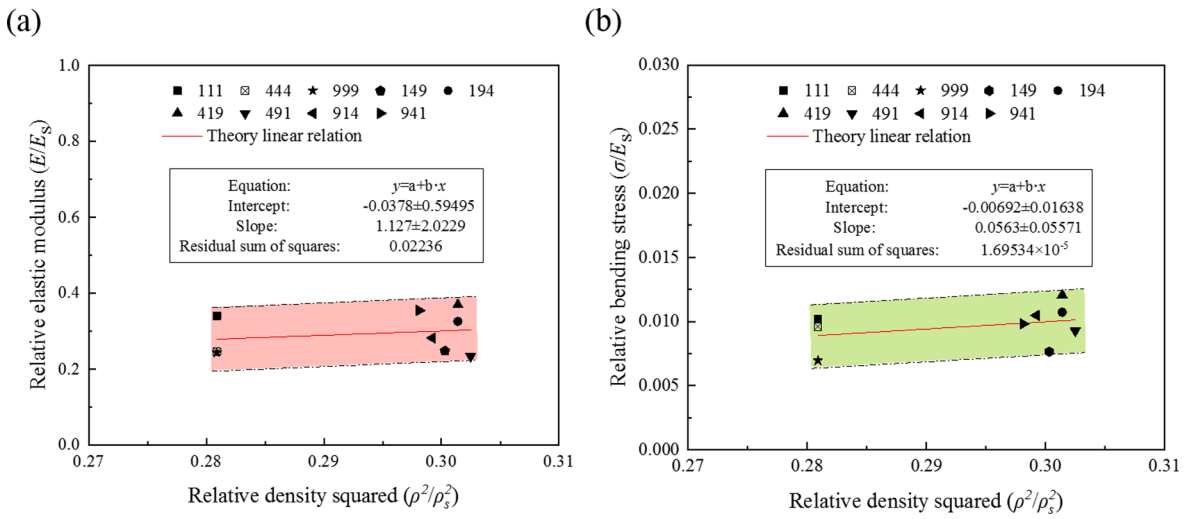

Fig. 5. Results contrast. (a) The relation between relative elastic modulus E/E_S and relative density ρ^2/ρ_S^2 of lattice structures. (b) The relation between bending stress σ/E_S and relative density ρ^2/ρ_S^2 of lattice structures.

$$f(\varepsilon) = A\varepsilon^k + B\left(1 - e^{-(E/C)\varepsilon(1-\varepsilon)^m}\right) + D\left(\frac{i\varepsilon}{1-\varepsilon}\right)^n \tag{19}$$

where,$A\varepsilon^k$, $B\left(1 - e^{-(E/C)\varepsilon(1-\varepsilon)^m}\right)$ and $D\left(\frac{i\varepsilon}{1-\varepsilon}\right)^n$ represent the elastic segment, the plateau segment and the dense segment of the lattice structures during compression.A,B, C and D are constants, which are related to the relative density.i,k, m and n are constants.

Due to the smoothness of$f(\varepsilon)$, the compression mutation caused by the local structural failure cannot be equivalent. The fracture failure factor $C(\varepsilon)$ is used to improve the smoothness of $f(\varepsilon)$ and improve accuracy.

$$C(\varepsilon) = \left|\sin\left(h\varepsilon^2\right)\right| \tag{20}$$

where, h is the constant.

Finally, Eq. (19) and Eq. (20) are substituted into Eq. (18) to obtain the constitutive relation.

$$\sigma = C(\varepsilon)f(\varepsilon) = \left|\sin\left(h\varepsilon^2\right)\right|\left(A\varepsilon^k + B\left(1 - e^{-(E/C)\varepsilon(1-\varepsilon)^m}\right) + D\left(\frac{i\varepsilon}{1-\varepsilon}\right)^n\right) \tag{21}$$

The simulated annealing algorithm [32], as shown in Fig. 6, is used to obtain the theoretical values of constitutive relation in the x and z directions. The academic data are shown in Table 2, Table 3, and Table 4.

RSS is the square of the correlation coefficient between the accurate and theoretical values.

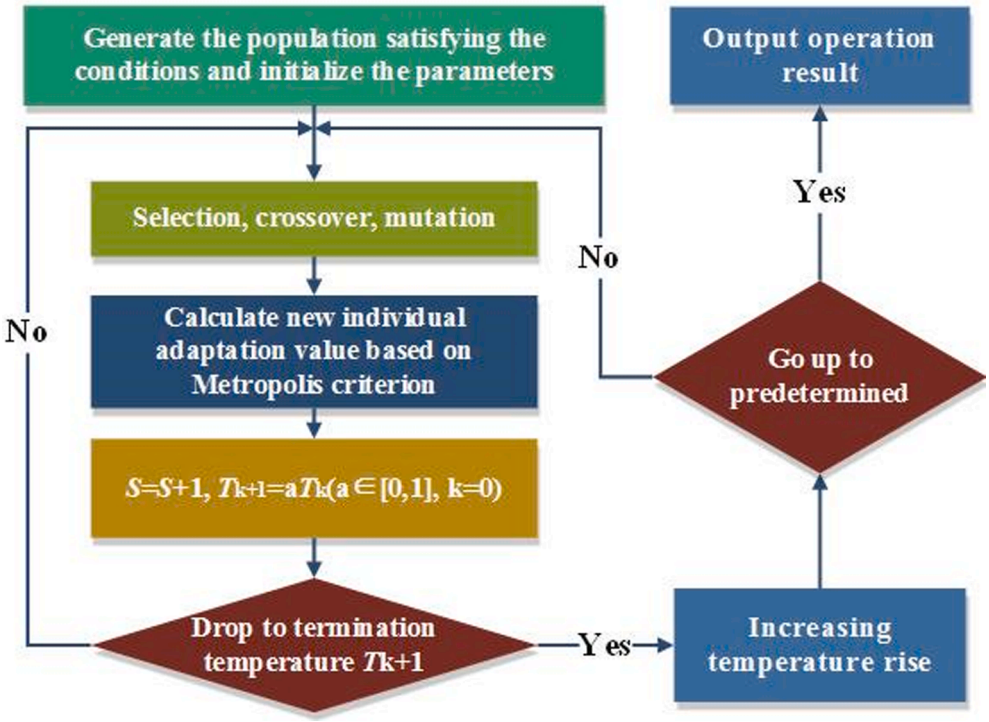

Fig. 6. Flow chart of Simulated annealing algorithm. The initial population is the initial input value.

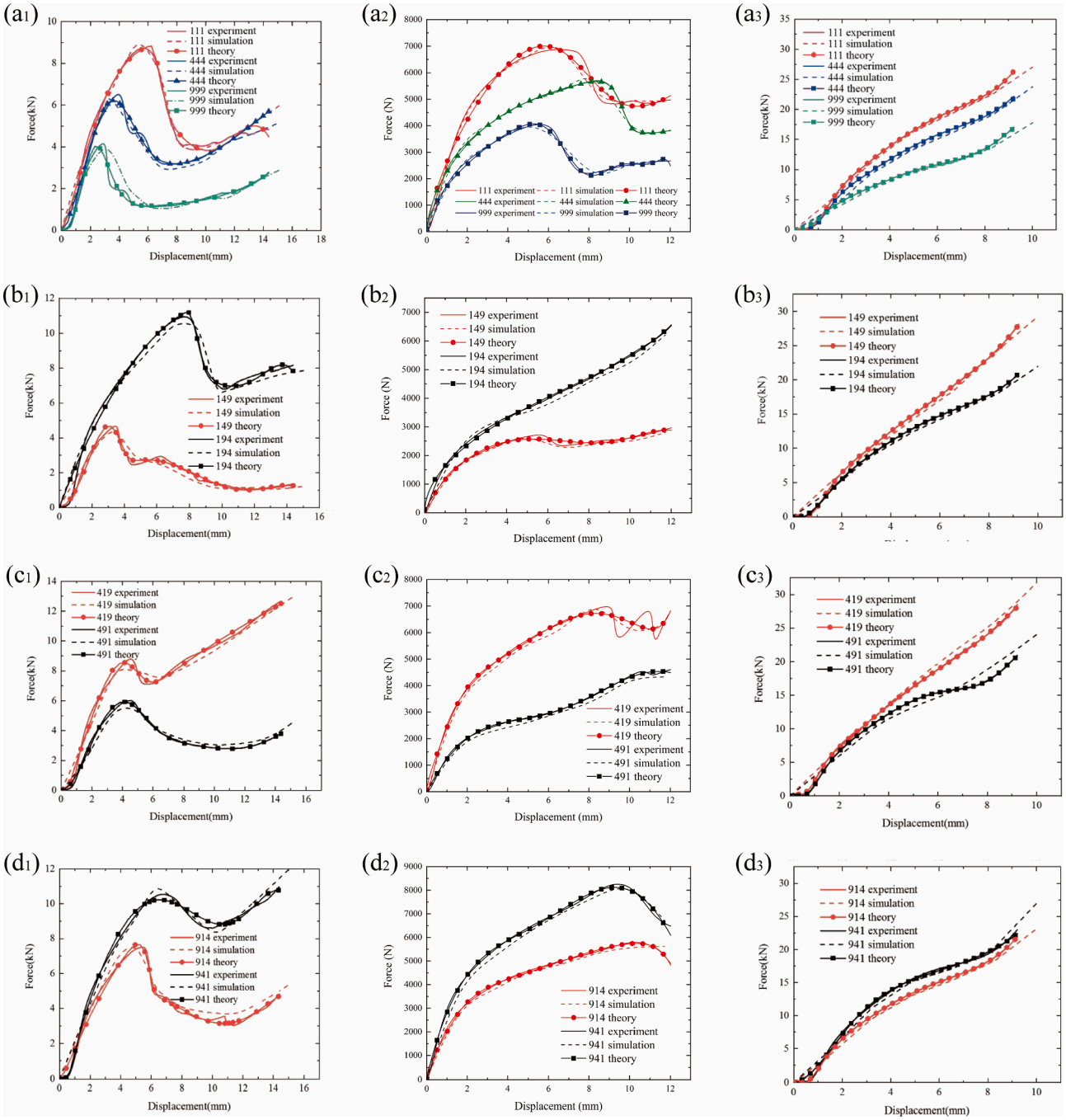

Fig. 7. Compressive mechanical curves of lattice structures.(a_1-d_1) x-direction compressive mechanical curves of lattice structures. (a_2-d_2) Oblique 45 degrees to the x-axis direction compressive mechanical properties curves of lattice structures. (a_3-d_3) z-direction compressive mechanical curves of lattice structures.

Table 2
x-direction theoretical value.

	A	*B*	*C*	*D*	*h*	*i*	*k*	*m*	*n*	RSS
111	689.128	−13.817	7.43	−1107.613	−11.804	3.718	−0.328	77.194	−0.221	0.988
444	4251.33	322.355	73.2	7.635	10.597	1.788	7.802	−4.321	−0.604	0.984
999	588.838	−545.305	0.464	−254.688	3.725	0.435	−0.903	55.278	−0.92	0.958
149	−7985.34	100.96	1835.864	7303.84	11.7	964	0.017	−30.186	0.0113	0.978
194	2285.35	−11.662	6.326	1211.445	11.662	78.730	5.736	68.243	−1.074	0.986
419	4364.44	209.833	160.581	0.1113	−10.26	0.003	6.972	−8.715	−0.814	0.993
491	−3413.7	209.654	126.323	3258.98	−7.976	1.677	0.049	−6.225	0.03	0.993
914	457.86	178.31	6198.004	−1032.17	2.716	4.054	−0.55	−21.35	−0.332	0.973
941	677.112	−67.983	−0.722	61.629	10.459	1.565	3.423	94.637	−0.715	0.995

Table 3
Oblique 45 degrees to the x-axis theoretical value.

	A	B	C	D	h	i	k	m	n	RSS
111	223.37	−67.131	0.749	7.796	2.192	3.429	1.657	−9.126	−1.263	0.988
444	221.467	−13.737	7.832	2.832	3.202	3.52	3.435	−47.465	−1.398	0.998
999	1.062	1.549	−0.0008	−1914.52	19.427	−3.295	−1.43	3.016	13.209	0.995
149	−5.665	6.551	13.157	1.908	9.777	3.091	−0.685	−7.152	−1.105	0.994
194	2.727	0.014	3.396	3.643	5.751	2.921	−1.495	37.346	2.491	0.998
419	2.337	536.153	79.337	−42.832	13.189	−15.04	−1.362	41.9	11.036	0.981
491	−50.061	−166.08	3.841	7.423	3.35	2.445	1.966	9.902	−1.046	0.998
914	22.537	3.554	−58.538	4.895	15.296	−7.002	−0.937	−11.548	−0.677	0.999
941	−1.147	7.132	−0.483	1.008	12.714	4.963	−1.740	−9.898	−1.498	0.998

Table 4
z-direction theoretical value.

	A	B	C	D	h	i	k	m	n	RSS
111	2505.78	−2422.47	18.791	15.821	3.308	0.386	7.532	−5.667	−0.924	0.99
444	456.597	−2350.107	28.806	241.9	2.039	5.244	5.083	−8.918	−0.954	0.99
999	4.66	4.053	−6.828	0.0044	10.704	4.587	−0.802	13.186	5.949	0.99
149	10.293	−1420.45	15.709	0.81	6.862	2.917	−1.089	−4.3	2.917	0.99
194	−561.681	975.82	39.388	1350.2	5.31	8.892	−0.437	1.56	−0.306	0.99
419	9.36	−1081.349	18.87	0.696	8.33	3.019	−1.082	−9.473	3.252	0.99
491	6.543	−1241.43	13.148	20.181	10.407	1.136	−1.117	−3.385	5.568	0.99
914	6.51	−2494.22	8.895	0.011	8.424	6.988	−1.219	0.691	3.911	0.99
941	1161.61	85.521	−16.955	−153.1	2.011	1	−0.216	11.04	−0.095	0.99

5. Lattice structures analysis

5.1. Evaluation indicators of lattice structures

This paper comprehensively describes the energy absorption and failure modes of cubic lattice structures. In the analysis of the corresponding results, the structural protection evaluation indicators are used: peak force (F_{max}), average force (F_{aver}), energy absorption (EA), specific energy absorption (SEA) and crush force efficiency (CFE).

Peak force (F_{max}) refers to the structural maximum bearing force during compression, as shown in Eq. (22). F_{max} determines the ultimate bearing capacity of cubic lattice structures, and the higher the F_{max}, the stronger the bearing capacity of cubic lattice structures [33].

$$F_{max} = \mathrm{Max}\{F\} \tag{22}$$

where, F is the structural force during compression. F_{max} is the maximum structural force during compression.

Average force (F_{aver}) is the structural average force under compression, as shown in Eq. (23). The average force's magnitude determines the structure's overall bearing capacity in the process of compression, and the larger the average force, the stronger the overall bearing capacity [34].

$$F_{aver} = \frac{\int_{x=0}^{x=x_0} F\mathrm{d}x}{x_0} \tag{23}$$

where, x_0 is the total compression displacement. F is the structural force during compression.

Energy absorption (EA) represents the overall energy absorption effect during compression. EA determines the energy conversion capacity of the broad structural protection. And the structural bearing capacity becomes better with the increase of EA [35].

$$EA = \int_{x=0}^{x=x_0} F\mathrm{d}x \tag{24}$$

Specific energy absorption (SEA) is the energy absorption of structural per unit mass, which is an actual structural design performance. The structural protection performance becomes better with the increase of SEA [36].

$$SEA = \frac{\int_{x=0}^{x=x_0} F\mathrm{d}x}{M_{str}} \tag{25}$$

where, M_{str} is the structural mass.

Crush force efficiency (CFE) is the ratio of F_{aver} toF_{max}, which is an actual performance of structural bearing stability. The closer the CFE is to 1, the better the structural strength is [32].

$$CFE = \frac{F_{aver}}{F_{max}} \tag{26}$$

5.2. Mechanical properties analysis of lattice structures

Differ in conventional single-direction compression experiments, the ×, oblique 45 degrees to the x-axis and z directions compression behaviors of lattice structures with the synergistic hierarchical arrangement are tested, as shown in Fig. 7.

Fig. 7 shows the mechanical properties of Nylon lattice structures with the synergistic hierarchical arrangement in different directions. The curves' coincidence degree of experimental, simulation, and theoretical results is highly consistent. The lattice structures compressed in the x direction exhibit secondary hardening effects, both in terms of initial modulus and secondary modulus after buckling strain. But the secondary hardening effect begins with the structural deformation, and the elastic deformation is the initial modulus. The initial compression deformation elastic segment structure, namely the initial modulus, reaches the yield stage. In the yield stage, the load transfer path is reduced due to crack propagation in structures. The force decreases. After the structural deformation reaches the yield stage, the crack propagates within the structural material, and the load transfer path is reduced. The bearing force is reduced. And a shear deformation failure occurs, prompting a reduction in the load-carrying capacity of the structure. With the increase of compression, the porosity of the lattice structure decreases. The cracks in the lattice structures close, and the overall force is stable. The lattice structure enters the second hardening stage.

The mechanical compression properties of the hybrid hierarchical and hierarchical synergies lattice structure in ×, oblique 45 degrees to the x-axis and z directions are in Fig. 8.

As can be seen from Fig. 7 (a_1-a_3) that the overall bearing capacity of

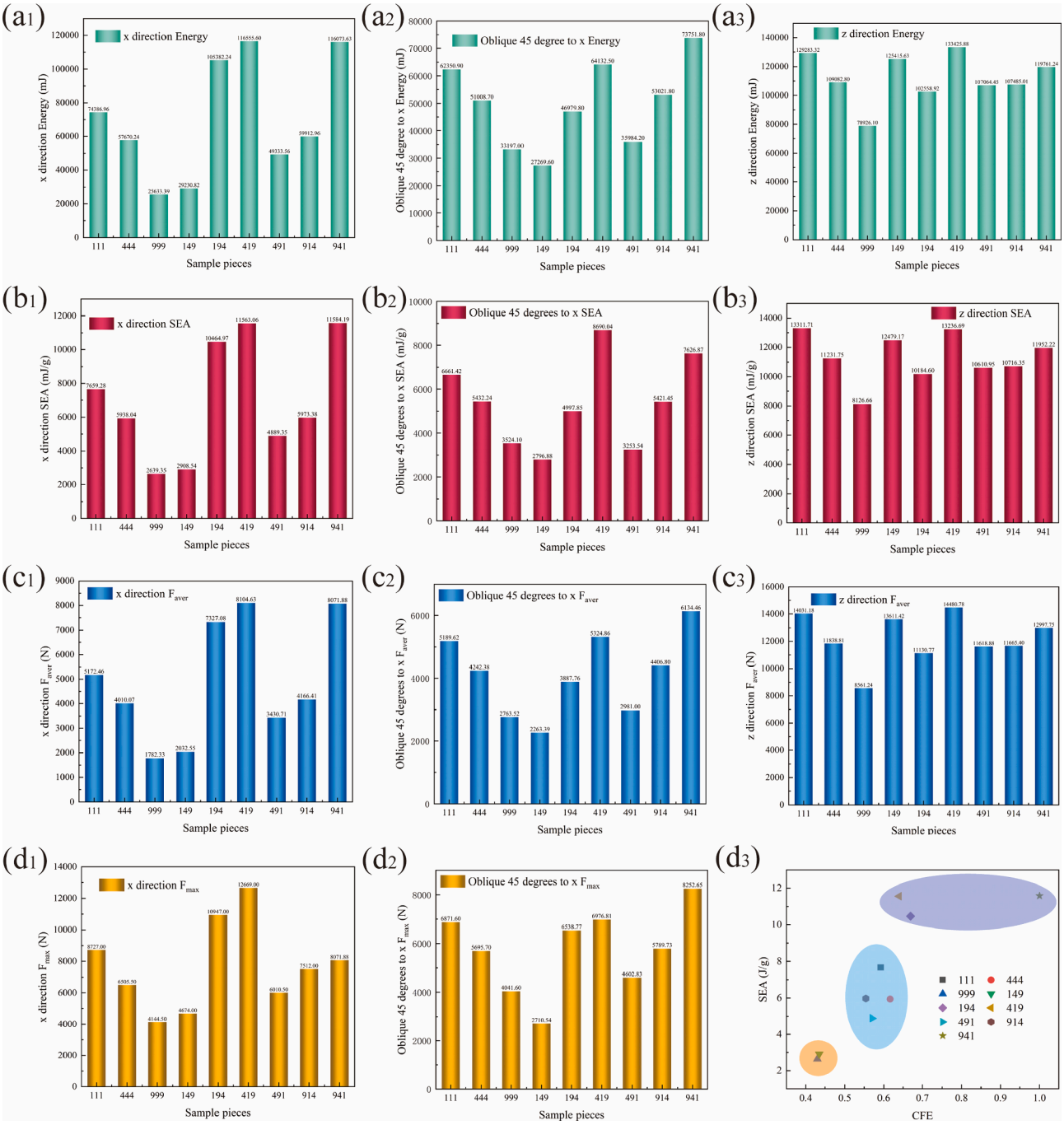

Fig. 8. Mechanical properties of lattice structures of synergistic hierarchical arrangement. (a_1-d_1) x-direction lattice structure compression *EA*, *SEA*, F_{aver}, F_{max}. (a_2-d_2) Oblique 45 degrees to the x-axis direction lattice structure compression *EA*, *SEA*, F_{aver}, F_{max}. (a_3-c_3) z-direction lattice structure compression *EA*, *SEA*, F_{aver}. (d_3) x-direction lattice structure compression *CFE-SEA*.

lattice structures can be reduced by hierarchical arrangement when the relative density remains unchanged. Still, the structural stability can be improved to some extent. The synergistic hierarchical arrangement can effectively improve lattice structures' bearing capacity and structural strength. In Fig. 8, a comparison of the compressive mechanical properties of hierarchical lattice structures shows that the hierarchical design can reduce the *EA* of lattice structures and improve load stability. Yet, the synergistic hierarchical arrangement can significantly improve the mechanical characteristics of lattice structures (*EA*, *SEA*, F_{max}, F_{aver}). The hybrid hierarchical lattice structures (194, 419 and 941) have the highest performance improved by the hybrid hierarchical arrangement. The *EA* of 194 hybrid hierarchical lattice structure, 419 hybrid hierarchical lattice structure, and 941 hybrid hierarchical lattice structure is 141.7 %, 156.7 %, 156.1 % of 111 hierarchical lattice structure, respectively. The *SEA* of 194 hybrid hierarchical lattice structure, 419 hybrid hierarchical lattice structure, and 941 hybrid hierarchical lattice structure is 136.6 %, 151 %, and 151.2 % of 111 hierarchical lattice structure, respectively. The *CFE* of 194 hybrid hierarchical lattice structure, 419 hybrid hierarchical lattice structure, and 941 hybrid hierarchical lattice structure is 113.6 %, 108.5 %, and 169.5 % of 111 hierarchical lattice structure, respectively. Among the hybrid hierarchical lattice structures, the 941 hybrid hierarchical lattice structure is consistent with the internal hybrid hierarchical distribution of the femoral structure and has the best mechanical properties.

Hierarchical and hybrid hierarchical synergies lattice structures have high SEA and CFE, and the comprehensive performance comparison is shown in Fig. 8 (d_3). The 941 hybrid hierarchical lattice structure has the best performance. The CFE of the 941 hybrid hierarchical lattice structure is about 1, which means that the 941 hybrid hierarchical lattice structure is exceptionally stable under compressive loads. Applying structures similar to the 941 hybrid hierarchical lattice structure in passenger transport safety can reduce violent impact and protect human safety. The SEA of 941 hybrid hierarchical lattice structure is 440 % of other hybrid hierarchical arrangement structures, which can absorb the external impact energy to the maximum extent. The results of lattice structures of synergistic hierarchical arrangement in this paper are taken as a reference to provide ideas for the application of energy absorption structures' manufacturing engineering and play a potential role in the engineering application of seat energy absorption block. To improve the survival rate of passengers in a traffic accident, the hybrid hierarchical lattice structure 941 can be arranged in the energy absorption block of the passenger seat.

5.3. Lattice structures' failure mode

Figs. 9 and 10 show deformation modes of lattice structures of synergistic hierarchical arrangement in the x direction, respectively. The simulated deformation results of the lattice structure agree with the experimental deformation in terms of the deformation pattern of the lattice structure, which further indicates that the simulation stress distribution is accurate.

As can be seen from the structural compression stress distribution in Fig. 9 (a_2), (b_2), and (c_2), the structural beams perpendicular to the compression direction are compressed first and plays a supporting role when the hierarchical lattice structure is compressed. The larger the supporting structure block, the better the lattice structure's bearing capacity. As the structural compression continues, the structural deformation increases and the cross parts of the structure (circled in red in Fig. 9 and Fig. 10) have shear action.

The stress distribution of the lattice structure is more uniform (the stress color distribution is more consistent) when the hybrid hierarchical lattice structure is compressed, as shown in Fig. 10. According to the compressive stress–strain contour of hierarchical and hybrid hierarchical lattice structures, it can be found that the hybrid hierarchical lattice structure can effectively disperse structural stress and reduce stress concentration.

6. Engineering application

When an automobile traffic accident happens, the passengers bear the energy input from the outside. Too much power is the key to passenger damage. Therefore, the car's back seat should absorb more energy from the passenger when the passenger is impacted. In this way, the energy in the passenger body can be effectively dissipated, thus achieving the goal of ensuring passenger safety. Among them, the lattice structure design of the automobile seat is an important means besides changing the strengthening material. Taking the Audi E-Tron car seat as an example, the steel ball compression test of the car seat filled with the hierarchical lattice structure is carried out. The hierarchical lattice structure is placed at the back of the back chair and fixedly connected with the back chair, as shown in Fig. 11.

In the car seat performance test, the car seat bottom is fixed; that is, the x, y, and z direction of the seat bottom and the three degrees of freedom of rotation around x, y, and z axis are completely constrained. The compression energy absorption test of automobile seats is carried out by moving the steel ball. The displacement of the steel ball is 16.01 mm, and the test time is 0.1 s. The experimental results are shown in Fig. 12.

As seen from the seat stress nephogram in Fig. 12, the stress distribution is the same when the steel ball compresses different seats. However, the high-stress concentration of the original seat can be observed at the compression center. The stress of the improved seats concentrates on both sides of the improved seats. The interlayer effectively disperses stress and dissipates energy effectively. The force shown in Fig. 12 (b_1) is the force change in the contact between the seat and the steel ball. Among them, the maximum force of 194 seat is 3960.1 N, the maximum force of 419 seat is 3912.5 N, and the ultimate force of 941 seat is 2718.9 N, which are 586.7 %, 578.4 %, 371.5 % of the original Audi E-Tron seat respectively. Squeezing the mezzanine seat at the same distance absorb more energy, of which, 194seat, 419 seat, and 941 seat absorb 463.9 %, 457.3 % and 287 % of the original Audi E-Tron seat, respectively. The improved seats can improve energy absorption capacity. When the body reclines and compresses the seat, it absorbs more energy to keep the body safe. The design ideas can be used in the microdesign material, with a wide range of applicability.

7. Conclusion

In this study, the hierarchical lattice cells are designed using the hierarchical concept. Based on the hierarchical cubic lattice cells, the hierarchical cubic lattices (111, 444, and 999) are composed for

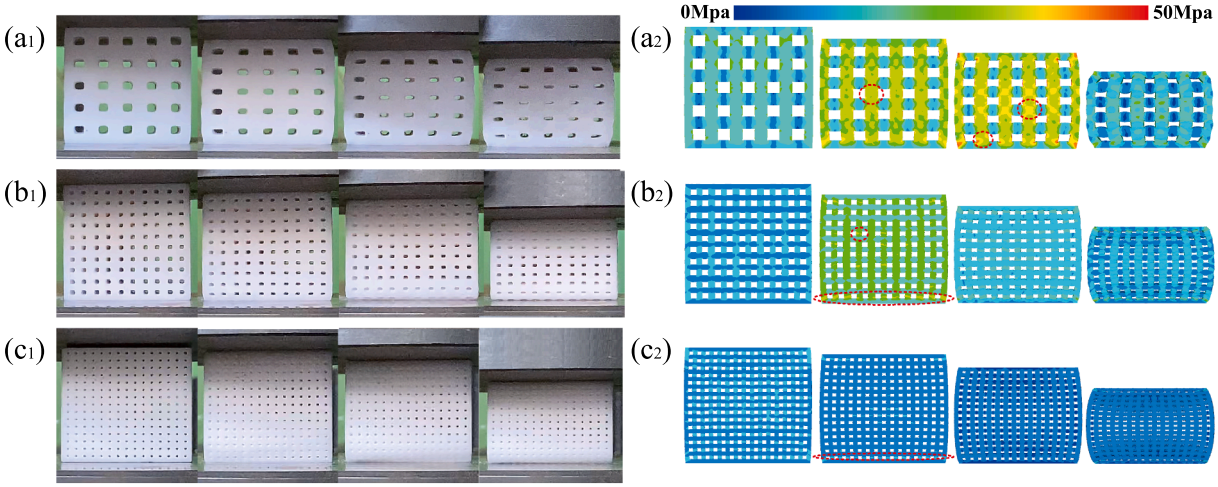

Fig. 9. Compression deformation modes of hierarchical lattice structures. The strain corresponding to the experimental and simulation figures from left to right is 0.062, 0.131, 0.200, and 0.323.

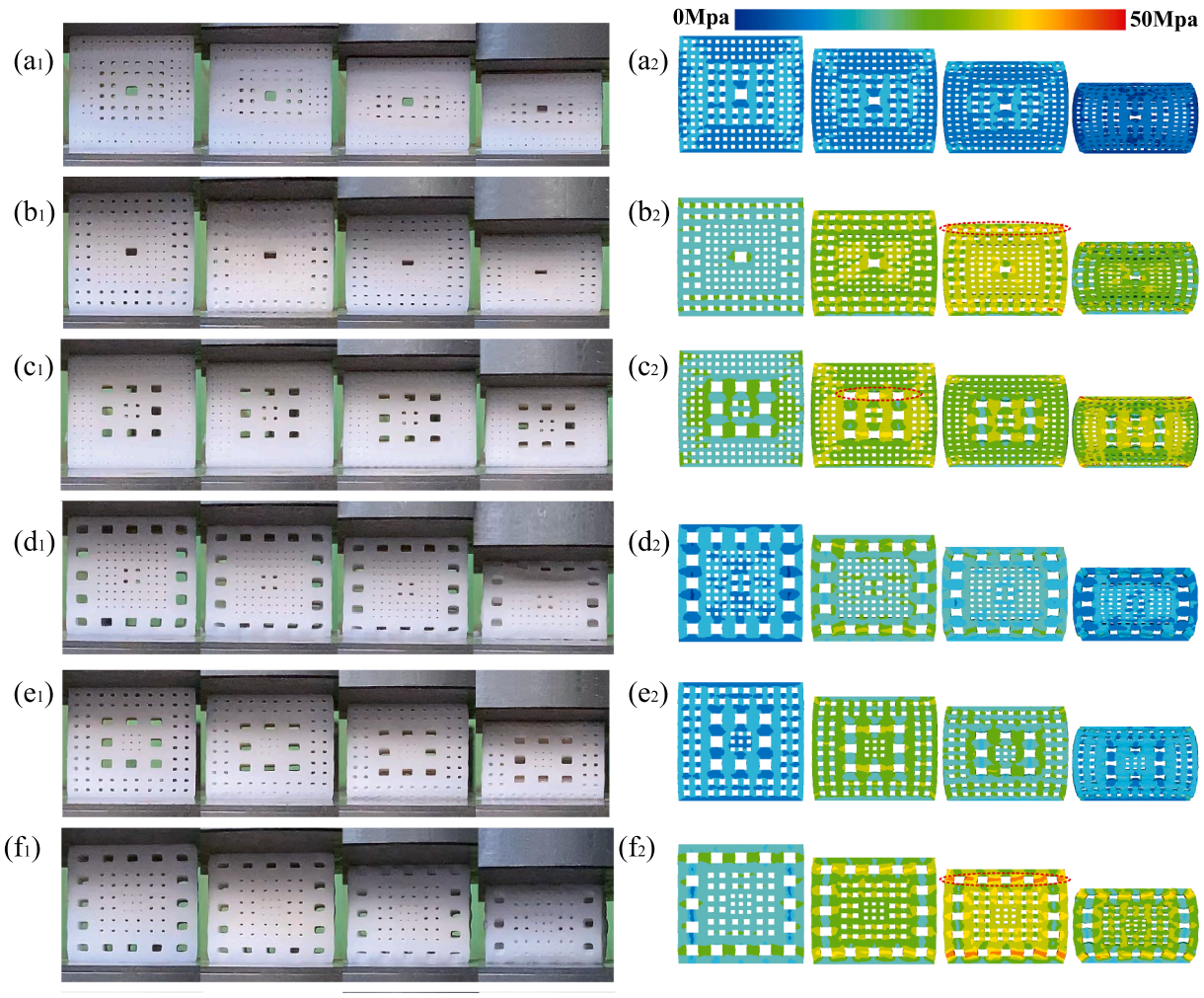

Fig. 10. Compression deformation modes of hybrid hierarchical lattice structures. The strain corresponding to the experimental and simulation figures from left to right is 0.062, 0.131, 0.200, and 0.323.

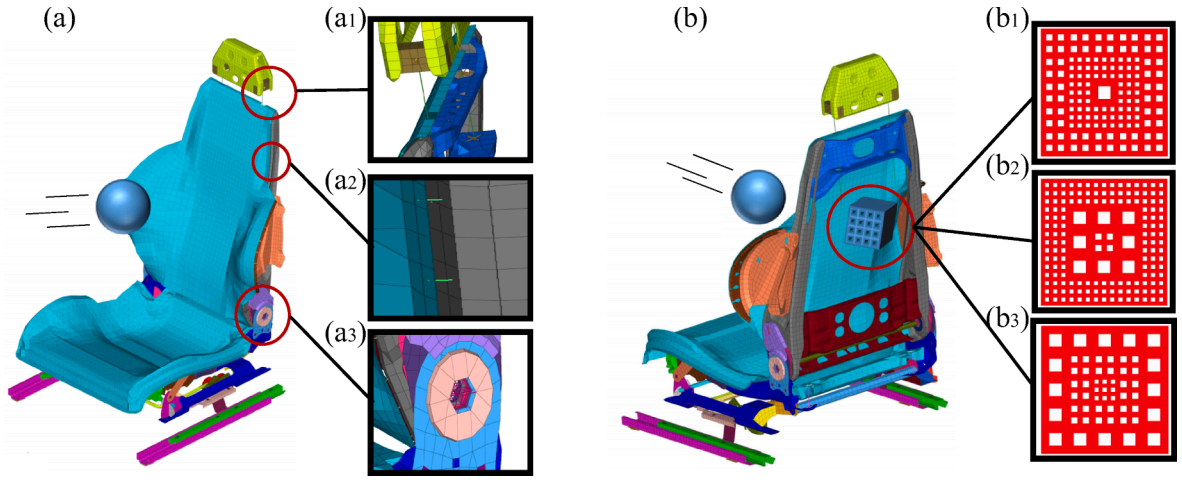

Fig. 11. Audi E-Tron car seat. (a) The view of Audi E-Tron car seat. (a_1) Head pillow connection. (a_2) Backrest part connection processing. (a_3) Seat rotation. (b) The rear view of Audi E-Tron car seat. (b_1) 194 hybrid hierarchical lattice structure. (b_2) 419 hybrid hierarchical lattice structure. (b_3) 941 hybrid hierarchical lattice structure.

studying the effect of hierarchical configuration on the overall mechanical properties of lattice structures. Next, to study the effect of the synergistic hierarchical arrangement on the mechanical properties, the lattice structures are arranged and combined to form the hybrid hierarchical lattice structures: 149, 194, 419, 491, 914, 941. The following conclusions are obtained by analyzing the mechanical properties of different directions and the cars' engineering applications.

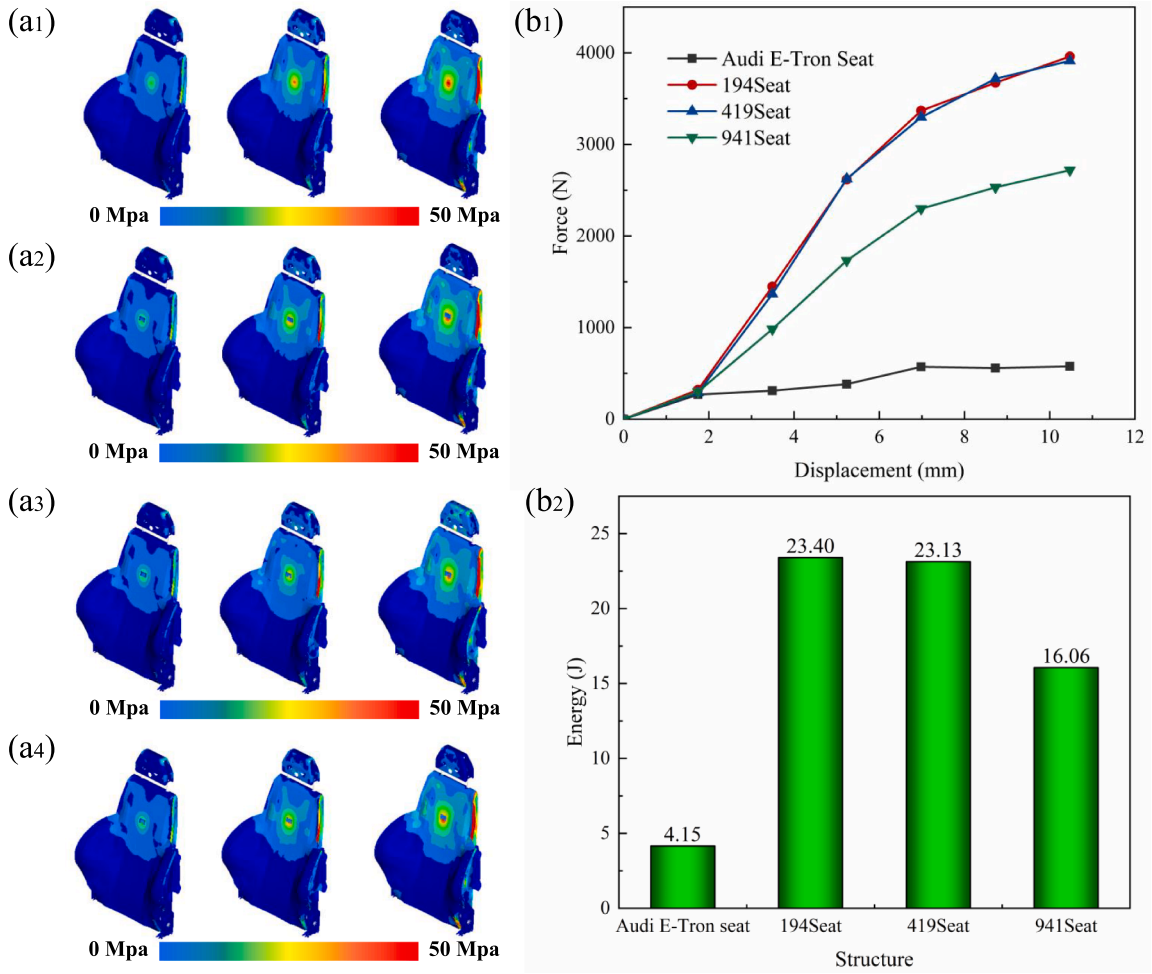

Fig. 12. Simulation results of the Audi E-Tron seat. (a_1) The stress nephogram of the Audi E-Tron seat of 1.75 mm, 6.98 mm, 11.05 mm. (a_2) The stress nephogram of the 194Seat of 1.75 mm, 6.98 mm, 11.05 mm. (a_3) The stress nephogram of the 419Seat of 1.75 mm, 6.98 mm, 11.05 mm. (a_4) The stress nephogram of the 941Seat of 1.75 mm, 6.98 mm, 11.05 mm. (b_1) The force–displacement curve of car seats. (b_2) The energy absorption diagram of car seats.

(1) The Euler predicted function and improved constitutive relation have a high degree of accuracy. The mechanical analysis results of the enhanced constitutive model obtained by the global simulated annealing optimization algorithm are very accurate compared to the experimental and simulation results, within 5 % error.
(2) When the mass of the lattice structures is the same, the hierarchical arrangement of the lattice structures will decrease the overall structural bearing capacity. The hierarchical arrangement of the lattice structure can improve compression stability. The synergistic hierarchical arrangement can effectively improve the bearing capacity of the lattice structures and make the lattice structures absorb more energy. In the x, oblique 45 degrees to the x-axis and z directions, 941 with a similar hybrid hierarchical arrangement inside the femur has the best mechanical properties. Its bearing capacity, specific energy absorption, energy absorption, and specific strength exceed 100 % of those of other lattice structures.
(3) The energy absorption effect of the car seat with the hybrid hierarchical lattice structure is 287 % higher than the original car seat. Hybrid hierarchical lattice structures can achieve excellent performance in engineering applications.

CRediT authorship contribution statement

Ruiyao Liu: Writing – original draft, Writing – review & editing, Visualization, Project administration, Data curation, Formal analysis, Methodology, Software, Formal analysis. **Guofeng Yao:** Writing – review & editing, Visualization, Supervision, Conceptualization, Validation. **Kuiyang Gao:** Writing – review & editing. **Zezhou Xu:** Writing – review & editing. **Yanan Yang:** Writing – review & editing. **Xue Guo:** Writing – review & editing. **Zhenglei Yu:** Writing – review & editing, Visualization, Funding acquisition, Resources, Conceptualization, Validation. **Zhihui Zhang:** Writing – review & editing. **Chunyang Han:** Writing – review & editing.

Declaration of Competing Interest

The authors declare that they have no known competing financial interests or personal relationships that could have appeared to influence the work reported in this paper.

Data availability

Data will be made available on request.

Acknowledgment

This research is funded by the National Natural Science Foundation of China (No. 51975246), the Science and Technology Development Program of Jilin Province (No. YDZJ202101ZYTS134), the Ascl-zytsxm (No. 202013), the Open Project Program of Key Laboratory for Cross-

Scale Mi-cro and Nano Manufacturing, Minstry of Education, Changchun University of Science and Technology (No. CMNM-KF202109), the Interdisciplinary Research Fund for Doctoral Postgraduates of Jilin University (No.101832020DJX052), Interdisciplinary Cultivation Project for Young Teachers and Students (No. 415010300078).

References

[1] Research for Crashworthiness of Aircraft Structures, National Aerospace Laboratory NLR [R]. NLR Annual Report; 2000.
[2] Namvar N, Zolfagharian A, Vakili-Tahami F, Bodaghi M. Reversible energy absorption of elasto-plastic auxetic, hexagonal, and AuxHex structures fabricated by FDM 4D printing. Smart Mater Struct 2022;31(5):055021.
[3] Juvan J, Prezelj I, Kopač E. Public dilemmas about security measures in the field of civil aviation[J]. Security Journal 2021;34(3):410–28.
[4] Dean JJ. BASH: Keeping Aviators Alive[J]. Mobility Forum 2021;30(2):18–9.
[5] Hamzehei R, Zolfagharian A, Dariushi S, Bodaghi M. 3D-Printed Bio-inspired Zero Poisson's Ratio Graded Metamaterials with High Energy Absorption Performance. Smart Mater Struct 2022;31(3):035001.
[6] Schuller E, Sperber M. Crash Safety in Aircraft Cabins[Z]. AIAA 1995:95–3978.
[7] Wang X, Qin RX, Chen BZ. Laser-based additively manufactured bio-inspired crashworthy structure: Energy absorption and collapse behaviour under static and dynamic loadings[J]. Mater Des 2021;211.
[8] Bodaghi M, Serjouei A, Zolfagharian A, Fotouhi M, Rahman H, Durandad D. Reversible energy absorbing meta-sandwiches by FDM 4D printing[J]. Int J Mech Sci 2022;173:10545.
[9] Abhirami AJ, Anup S. Mechanical properties of unidirectional bio-inspired composites with two non-self-similar hierarchical structures[J]. Mech Mater 2021;163.
[10] Yao GF, Liu RY, Xu ZZ, Xin RL, Chen LX, Yu ZL, et al. Study on quasi-static mechanical properties of four 3D-printed bio-inspired structures based on functional relationship[J]. Compos Struct 2021;274.
[11] Clément A, Julien CJ, Linares JM, Lopez QA. Bio-inspired method based on bone architecture to optimize the structure of mechanical workspieces[J]. Mater Des 2018;160:708–17.
[12] Shaan C, Dominique H, Hornez JC, Anne L, Francis C. Bio-inspired hydroxyapatite dual core-shell structure for bone substitutes[J]. J Eur Ceram Soc 2017;37(16):5321–7.
[13] Liang JH, Song R, Huang QL, Yang Y, Lin LX, Zhang YM, et al. Electrochemical construction of a bio-inspired micro/nano-textured structure with cell-sized microhole arrays on biomedical titanium to enhance bioactivity[J]. Electrochim Acta 2015;174:1149–59.
[14] Rahman H, Yarali E, Zolfagharian A, Serjouei A, Bodaghi M. Energy Absorption and Mechanical Performance of Functionally Graded Soft-Hard Lattice Structures [J]. Materials 2021;14(1366):1366.
[15] Torres Y, Trueba P, Pavón JJ, Chicardi E, Kamm P, García-Moreno F, et al. Design, processing and characterization of titanium with radial graded porosity for bone implants[J]. Mater Des 2016;110:179–87.
[16] Chen B, Yin DG, Yuan Q, Luo J, Fan JH. Microstructural mechanism of high rigidity and high strength of unio douglasiae shell[J]. Chinese Journal of Rare Metal and Engineering 2011;40(S1):69–72.
[17] Kooistra GW, Deshpande V, Wadley HNG. Hierarchical corrugated core sandwich panel concepts[J]. J Appl Mech 2007;74(2):259–68.
[18] Katayama T, Yamamoto H, Nozato T. Development of solid-fluid biomimetic composites load dispersion effect of controlled hydrostatic pressure[J]. Advances in Materials Processing Technologies 2001;119(4):65–71.
[19] Maliaris G, Argyros A, Smyrnaios E, Michailidis N. Novel additively manufactured bio-inspired 3D structures for impact energy damping[J]. CIRP Annals-Manufacturing Technology 2021;70(1):199–202.
[20] J Eng 2020.
[21] Du YX, Gu DD, Xi LX, Dai DH, Gao T, Zhu JH, et al. Laser additive manufacturing of bio-inspired lattice structure: Forming quality, microstructure and energy absorption behavior[J]. Mater Sci Eng, A 2020;773.
[22] Yan CZ, Liang H, Ahmed H, Philippe Y, David R. Advanced lightweight 316L stainless steel cellular lattice structures fabricated via selective laser melting[J]. Mater Des 2014;55:533–41.
[23] Maskery I, Aboulkhair NT, Aremu AO, Tuck CJ, Ashcroft IA, Wildman RD, et al. A mechanical property evaluation of graded density Al-Si10-Mg lattice structures manufactured by selective laser melting[J]. Mater Sci Eng, A 2016;670:264–74.
[24] Gorny B, Niendorf T, Lackmann J, Thoene M, Troester T, Maier HJ. In situ characterization of the deformation and failure behavior of non-stochastic porous structures processed by selective laser melting[J]. Mater Sci Eng, A 2011;528(27):7962–7.
[25] Marvan J, Horak Z, Bartoska R, Kachlik D, Dzupa V, Baca V. Osteon directions in compact bone of distal part of the human fibula: Morphological and biomechanical aspects[A]. Chinese Society for Anatomical Sciences. Abstracts of the 18th Congress of the International Federation of Associations of Anatomists(IFAA 2014)[C].Chinese Society for Anatomical Sciences, 2014: 1.
[26] Subbiah R, Bensingh J, Kader A, Nayak S. Influence of printing parameters on structures, mechanical properties and surface characterization of aluminium alloy manufactured using selective laser melting[J]. The International Journal of Advanced Manufacturing Technology 2020;106(11):5137–47.
[27] Gibson LJ, Ashby MF. Cellular solids: Structure and properties[M]. Pergamon Press; 1997.
[28] Avalle M, Belingardi G, Ibba A. Mechanical models of cellular solids: Parameters identification from experimental tests[J]. Int J Impact Eng 2006;34(1):3–27.
[29] Nagy A. Mechanical Behavior of Foamed Materials Under Dynamic Compression [J]. J Cell Plast 1974;10(3):127–34.
[30] Jankowski M, Czechowski L, Kotełko M. Numerical simulation of energy absorption in polyurethane foams under impact[J]. Journal of Kones 2015;19(4):245–52.
[31] Jeong KY, Cheon SS, Munshi MB. A constitutive model for polyurethane foam with strain rate sensitivity[J]. J Mech Sci Technol 2012;26(7):2033–8.
[32] Holman OM, Leonardo AQJ, Francisco JL, Shyrle BG, Lope HB, Shib SS. Extraction of decision rules using genetic algorithms and simulated annealing for prediction of severity of traffic accidents by motorcyclists[J]. J Ambient Intell Hum Comput 2021:1–22.
[33] Park JM, Wang G, Pauly S, Mattern N, Kim DH, Eckert J. Ductile Ti-Based Bulk Metallic Glasses with High Specific Strength[J]. Metallurgical & Materials Transactions Part A 2011;42(6):1456–62.
[34] Yin HF, Zheng XJ, Wen GL, Zhang C, Wu ZT. Design optimization of a novel bio-inspired 3D porous structure for crashworthiness[J]. Compos Struct 2021;255.
[35] Lehmann E, Peschmann J. Energy absorption by the steel structure of ships in the event of collisions[J]. Mar struct 2002;15(4):429–41.
[36] Lee JH, Wang L, Boyce MC, Thomas EL. Periodic Bicontinuous Composites for High Specific Energy Absorption[J]. Nano Lett 2012;12(8):4392–6.